Joule

CellPress

Article

Detection of Micro-Scale Li Dendrite via H_2 Gas Capture for Early Safety Warning

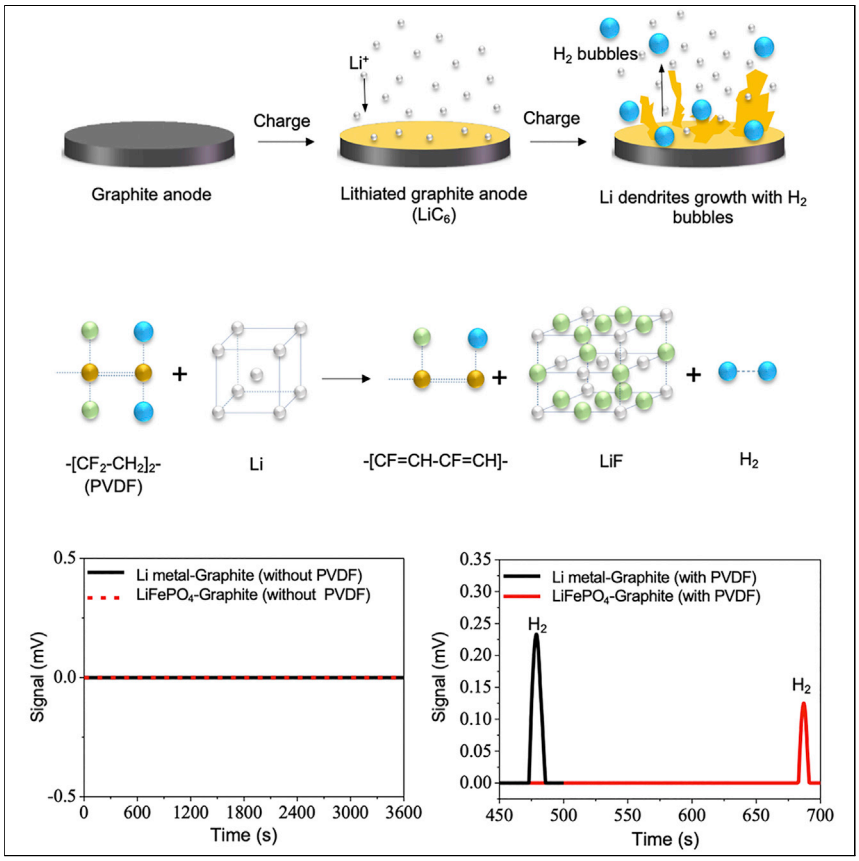

Li dendrite growth is a critical and predominant reason for separator piercing and cell shorts and is very difficult to detect in the early state. Here, we developed a new sensitive detection method based on hydrogen (H_2) gas capture generated from reaction of metallic Li with polymer binders. The proposed method could detect trace amounts of Li-metal formation down to the micron scale for very early safety warnings, which could help improve battery safety.

Yang Jin, Zhikun Zheng, Donghui Wei, ..., Yang Liu, Jinfeng Gao, Yi Cui

yangjin@zzu.edu.cn (Y.J.)
yicui@stanford.edu (Y.C.)

HIGHLIGHTS

Micron-scale Li dendrite (~2.8 × 10^{-4} mg, 50 μm) growth can trigger H_2 capture

The battery pack surface temperature was still very low (35.6°C) when H_2 captured

The H_2 gas capture time was 639 s earlier than smoke and 769 s earlier than fire

The Li dendrite growth and thermal runway could be prevented once H_2 captured

Jin et al., Joule 4, 1–16
August 19, 2020
https://doi.org/10.1016/j.joule.2020.05.016

Please cite this article in press as: Jin et al., Detection of Micro-Scale Li Dendrite via H_2 Gas Capture for Early Safety Warning, Joule (2020), https://doi.org/10.1016/j.joule.2020.05.016

Joule

CellPress

Article

Detection of Micro-Scale Li Dendrite via H_2 Gas Capture for Early Safety Warning

Yang Jin,[1,*] Zhikun Zheng,[1] Donghui Wei,[2] Xin Jiang,[1] Hongfei Lu,[1] Lei Sun,[3] Fengbo Tao,[3] Dongliang Guo,[3] Yang Liu,[3] Jinfeng Gao,[1] and Yi Cui[4,5,6,*]

SUMMARY

Li-ion battery safety issues related to fires and explosions are frequently triggered by Li dendrite growth, which is a predominant reason for separator piercing and cell shorts and is very difficult to detect in the early state. Here, we developed a sensitive detection method based on H_2 gas capture that could detect trace amounts of Li dendrite formation. H_2 gas was generated due to reaction of metallic Li with polymer binders. Even micron-scale Li dendrite (~2.8 × 10^{-4} mg and 50 μm) growth can trigger H_2 capture. Overcharge experiment with a $LiFePO_4$-graphite battery pack (8.8 kWh) shows that H_2 was captured first among H_2, CO, CO_2, HCL, HF, and SO_2, and the capture time was 639 s earlier than smoke and 769 s earlier than fire. The Li dendrite growth can be completely prevented once H_2 is captured, with neither smoke nor fire observed, which provides an effective method for early safety warning.

INTRODUCTION

In recent years, the development of electrochemical energy storage technology has received extensive attention. Lithium(Li)-ion batteries (LIBs) have become one of the most competitive electrochemical energy storage technologies for portable devices, electric vehicles, and stationary energy storage due to their high energy density and reduced cost.[1–3] State-of-the-art LIBs can reach specific energy of ~250 Wh kg^{-1}, and greater energy density technology beyond 500 Wh kg^{-1} (1,800 kJ kg^{-1}) is under exploration worldwide. However, due to the flammable organic electrolytes and the intrinsic thermal properties during charge and discharge,[4–6] LIB safety accidents, called battery thermal runaway, frequently occur due to Li dendrite growth on graphite anodes under overcharging or fast charging situations,[7] necessitating an effective method to detect Li-metal dendrites as early as possible.[8–11]

LIBs are composed of electrodes (Li-metal-oxide cathode and graphite anode), a polymer separator, and a liquid electrolyte (containing Li salt and an organic solvent) and are usually sealed in an aluminum, stainless-steel or plastic package.[12] The above sealing materials and design inevitably lead to poor thermal dissipation considering that the battery intrinsically produces joule heat during charging or discharging, especially under extreme conditions such as overcharging or fast charging situations where Li dendrite grow on the graphite anode and pierce the polymer separator.[13,14] A large amount of heat is easily produced inside a dendrite-shorted battery, which can subsequently increase the internal temperature and induce additional violent exothermic chemical reactions for further heat generation, producing vast quantities of gases and even resulting in catastrophic fire.[15–18] For stationary

Context & Scale

State-of-the-art Li-ion batteries (LIBs) can reach a specific energy of ~250 Wh kg^{-1}, and greater energy density technology beyond 500 Wh kg^{-1} (1,800 kJ kg^{-1}) is under exploration worldwide. However, due to the flammable organic electrolytes and the intrinsic thermal properties, LIB safety accidents frequently occur due to Li dendrite growth on graphite anodes under overcharging or fast charging situations, necessitating an effective method to detect Li-metal dendrites as early as possible. Here, we developed a new sensitive detection method based on hydrogen gas capture that could detect trace amounts of Li-metal formation down to the micron scale for very early safety warnings. H_2 gas was generated upon the growth of very small amounts of Li metal due to the reaction of metallic Li with polymer binders. Even micron-scale Li dendrite metal (~50 μm) growth on a graphite anode can generate enough H_2 gas to be captured for early safety warning, which could help improve battery safety.

energy storage, thousands of LIB cells are stacked in an energy storage cabin (molecular weight [MW] level), and the safety conditions are more severe. Therefore, exploration of early detection methods for Li-metal dendrite formation is critical to prevent safety accidents.[19]

The existing safety warning system of LIB-based BESS (battery energy storage system) mainly relies on special gas detection, smoke detection, and battery management system (BMS) protection. For gas detection, CO and hydrocarbons have been regarded as effective indicators for safety warning (heat abuse or overcharge condition).[20–22] However, the above gases come from the reduction and oxidation of the electrolyte or solid electrolyte interface (SEI) decomposition (>90°C)[18,23,24] and cannot serve as indicators during the Li dendrite growth period when battery internal temperature is low (<50°C), and thermal runway has not yet occurred. Smoke detectors send an alarm signal when a fire has already broken out and cannot realize the function of early safety warnings.[23,25] BMSs are regarded as crucial battery protection systems for safety accidents, such as thermal runway.[26] Current BMS can detect the battery cell external surface temperature, voltage, and state of charge (SOC), thus protecting a battery from overcharge and sending an alarm signal if the battery external temperature exceeds the normal range.[24] However, the SOC estimation precision is not sufficient, and the error rate increases in a large battery capacity environment (such as MW-level BESS).[27–29] There is a large difference between the battery internal and external temperatures due to the poor thermal conduction of many cell components.[30–32] Thus far, SOC and external temperature measurements have been unable to detect the Li dendrite growth and prevent battery safety failure, causing many recent catastrophic events (Tesla electric car battery fire and Samsung Note 7 fires and explosions). A more reliable method is needed that can precisely and timely perceive safety issues in a very early Li dendrite growth stage as a warning and allow enough time for precautions, such as personnel evacuation and cutting off chargers.

It is reported that various techniques were developed for Li dendrite detecting, such as *in situ* X-ray,[33] *in situ* Raman,[34] *in situ* neutron diffraction,[35] electron paramagnetic resonance (EPR),[36] and nuclear magnetic resonance (NMR) spectroscope,[37] etc., which enable to obtain information about the Li dendrite morphologies, formation mechanism, and quantitative descriptions. However, the added manufacturing complexity making it differs from actual battery structure, and the dependent expensive equipment retards its large-scale application. Other indirect strategies were proposed, such as detecting Li plating on anode by external electrochemical characteristic (voltage, capacity, etc.),[38–40] while data error is unavoidable and the complex criteria enhances incompatibility with BMS. Despite the high importance, so far, no analytical technique compatible with current battery manufacturing technique has been practically realizable for physically and directly detecting Li dendrite growth without extra battery structural modification.

Here, we, for first time, propose a detection method for micron-scale Li dendrites by H_2 gas capture for very early safety warning. This method relies on the spontaneous reaction between Li-metal and common electrode polymer binders, such as polyvinylidene difluoride (PVDF) or styrene-butadiene rubber (SBR) and carboxymethylcellulose (CMC), which produces H_2 gas at a very early stage. While H_2 gas is released from battery cell through valve, it can be captured by H_2 gas sensor immediately and serve as an effective abnormal indictor of Li-metal formation for early safety warning. The proposed technique works without changing the commercial LIBs structure and is compatible with existing BMS as it serves as independent

[1]Research Center of Grid Energy Storage and Battery Application, School of Electrical Engineering, Zhengzhou University, Zhengzhou 450001, P. R. China

[2]College of Chemistry, and Institute of Green Catalysis, Zhengzhou University, Zhengzhou 450001, P. R. China

[3]State Grid Jiangsu Electric Power CO., LTD. Research Institute, Nanjing 211103, P. R. China

[4]Department of Materials Science and Engineering, Stanford University, Stanford, CA 94305, USA

[5]Stanford Institute for Materials and Energy Sciences, SLAC National Accelerator Laboratory, 2575 Sand Hill Road, Menlo Park, CA 94025, USA

[6]Lead Contact

*Correspondence: yangjin@zzu.edu.cn (Y.J.), yicui@stanford.edu (Y.C.)

https://doi.org/10.1016/j.joule.2020.05.016

Please cite this article in press as: Jin et al., Detection of Micro-Scale Li Dendrite via H_2 Gas Capture for Early Safety Warning, Joule (2020), https://doi.org/10.1016/j.joule.2020.05.016

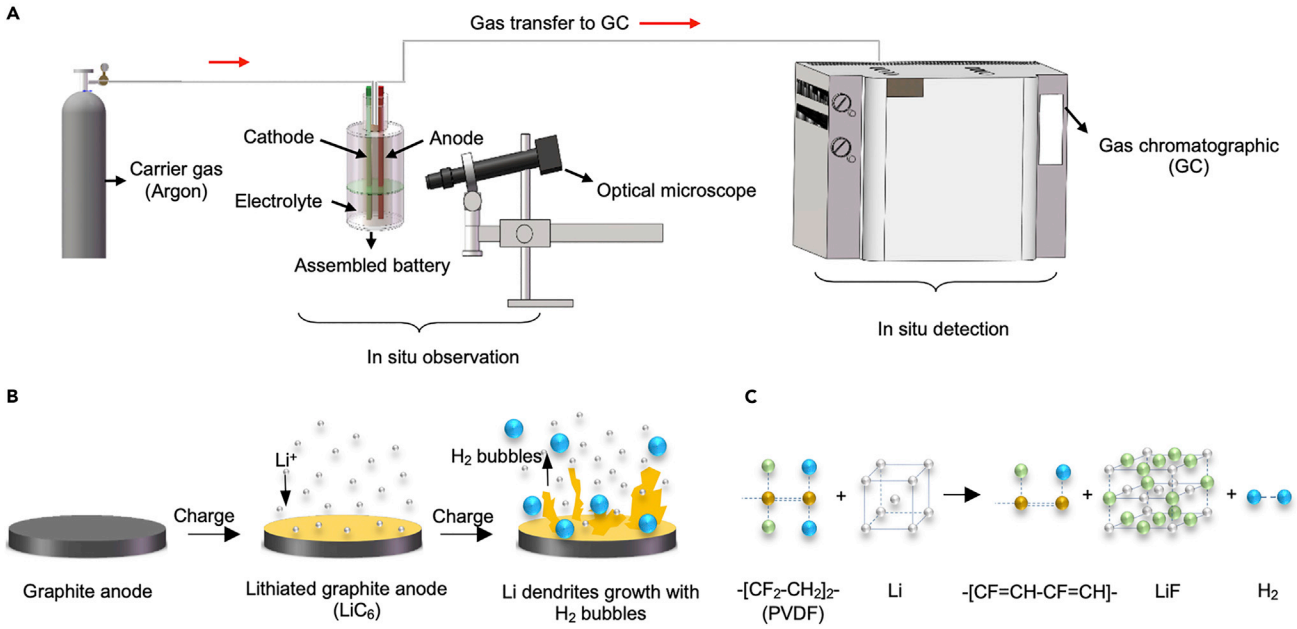

Figure 1. Schematic of Li Dendrite Growth Detection by H_2 Gas Capture

(A) Illustration of the *in situ* optical observation of Li dendrite growth and *in situ* capture of H_2 gas.

(B) Illustration of the H_2 gas generation mechanism. Li dendrites react with the PVDF binder, thus generating H_2 gas.

(C) Chemical reaction mechanism of Li dendrites and PVDF binder.

warning criteria. The technological maturity of H_2 gas sensor reduces the installation cost and complexity.[41] Next, we will study the reaction mechanism through *in situ* optical observation and H_2 gas capture experiment and verify the practical application through overcharge and warning experiment of commercial LIB packs (both prismatic and pouch cells) and clusters in real BESS cabin.

RESULTS

Schematic of Li Dendrite Growth Detection by H_2 Gas Capture

An *in situ* optical observation and H_2 gas capture platform was built to demonstrate the schematic of Li dendrite growth detection by H_2 gas capture. As shown in Figure 1A, the gas generated by a self-assembled LIB, which consists of a Li iron phosphate ($LiFePO_4$) cathode, graphite anode, EC (ethylene carbonate), EMC(ethyl methyl carbonate) and PC(propylene carbonate) electrolyte sealed in a glass bottle, was carried into a gas chromatograph and detected automatically (with argon as the carrier gas). The dendrite formation behavior can be recorded by optical microscopy simultaneously. In normal situations, Li ions are deintercalated from the cathode and intercalated into the graphite anode with LiC_6 formation.[42] Under overcharge or fast charge conditions, Li dendrites start growing on Li-saturated parts of graphite anode and react with polymer binder thus generating H_2 gas (Figure 1B).

The Li-PVDF reaction is expressed in Figure 1C. Here, the density functional theory (DFT) calculations were performed using the Gaussian16 program[43] to study the reaction kinetic of Li-metal and PVDF binder. B3LYP[44,45] method and basis set 6–31G(d,p) were employed for all atoms involved in the model reaction. The solvent effect was considered by using the IEFPCM model[46,47] and setting dielectric constant as 2.9 for all kinds of calculations. After the structural optimizations for all the stationary points, frequency calculations at the same level of theory were carried

out to identify all of the stationary points as minima (zero imaginary frequency) or transition state (only one frequency) and to provide corrections for free energies. As shown in Figure S1, there are three steps for the structural transformation from $CH_3CF_2CH_2CHF_2$ and Li_2 to CH_2=CFCH=CHF, two molecules of LiF, and one molecule of H_2. The first step is the abstraction of F^- by Li_2 via transition state TS1 with an energy barrier of 10.5 kcal mol^{-1}. The second step is the abstraction of a proton by Li_2F via transition state TS2 with an energy barrier of 21.0 kcal mol^{-1}. The third step is the abstraction of F^- and H^+ by HLi_2F coupled with the dissociation of a molecule of H_2 and two molecules of LiF via transition state TS3 with an energy barrier of 24.1 kcal mol^{-1}. The DFT calculation results theoretically demonstrate the reaction mechanism of Li metal and PVDF binder at room temperature ambient.

It is well known that during the first few cycles of LIBs, side chemical reactions take place to form the SEI layer.[48,49] In PC- and EC-based solvents with common inorganic salts, such as $LiPF_6$, electrolyte reduction occurs with a graphite electrode <0.9 V and is accompanied by gassing.[50] This process is called "battery formation." Different gases, such as CH_4,[51] C_2H_2,[15] C_2H_4,[52] C_3H_6,[52] CO,[51] and CO_2,[51,53,54] are generated from the reduction of EC and PC solvents during the formation. H_2 gas can be generated if there are water impurities in the electrolyte,[55] but water will be consumed quickly and can no longer generate H_2 after formation; thus, the H_2 gas will be vented before resealing.[56] To further eliminate the trace water impurities, the fabricated cells in our experiments had been pre-cycled multiple times (SEI already formed) with purging the cell simultaneously by high purity Ar (99.999%) carrier gas until no H_2 signal is detected. After the possible interfering, H_2 gas was totally purged, the cell could be used for the Li dendrite detection experiment.

In Situ Experiments of Li Dendrite Detection and H_2 Gas Capture with Polymer Binder

It is important to prove that H_2 gas comes from the reaction of dendrites and polymer binder. *In situ* experiments were carried out through above platform as seen in Figure 1A (optical image in Figures S2 and S3). $LiFePO_4$-graphite and Li metal-graphite are used as electrodes, respectively, to exclude the effect of $LiFePO_4$ cathode. Both graphite anodes contained PVDF and carbon black, which were pre-dried by a vacuum drier, and the mass ratio of graphite:carbon black:PVDF was 8:1:1. The distance between two electrodes was about 5 mm. The active anode and cathode electrode area were both 3 cm^2. The theoretical area capacity of graphite anode was 1 mAh cm^{-2}, and the charging current density was 1 mA cm^{-2} (equivalent to 1 C rate).

Figure 2A shows the cell voltage profile during charging. For the $LiFePO_4$-graphite cell, charging process starts from 0% SOC at 0 s, and Li dendrite growth was observed at approximately 683 s. The cell voltage was approximately 3.6 V. Due to the relatively high cell overpotential and more concentrated current density on electrode edge (simulation of current density distribution in Figures S4–S6), Li is more easily to be deposited on electrode edge, and Li dendrites start growing at early charging state (~10% SOC). At the same time, a H_2 gas signal was detected (Figure 2B) by gas chromatography, and H_2 bubbles were observed by optical microscopy (Video S1) simultaneously. No CO signal was detected during the Li dendrite growth. Due to the resolution limitation of microscopy, the initial dendrite can be smaller than 1 μm and forms much earlier than 683 s. For the Li-metal-graphite cell, charging process also starts from 0% SOC at 0 s, and Li dendrite growth was observed at approximately 472 s, while the cell voltage was

Please cite this article in press as: Jin et al., Detection of Micro-Scale Li Dendrite via H_2 Gas Capture for Early Safety Warning, Joule (2020), https://doi.org/10.1016/j.joule.2020.05.016

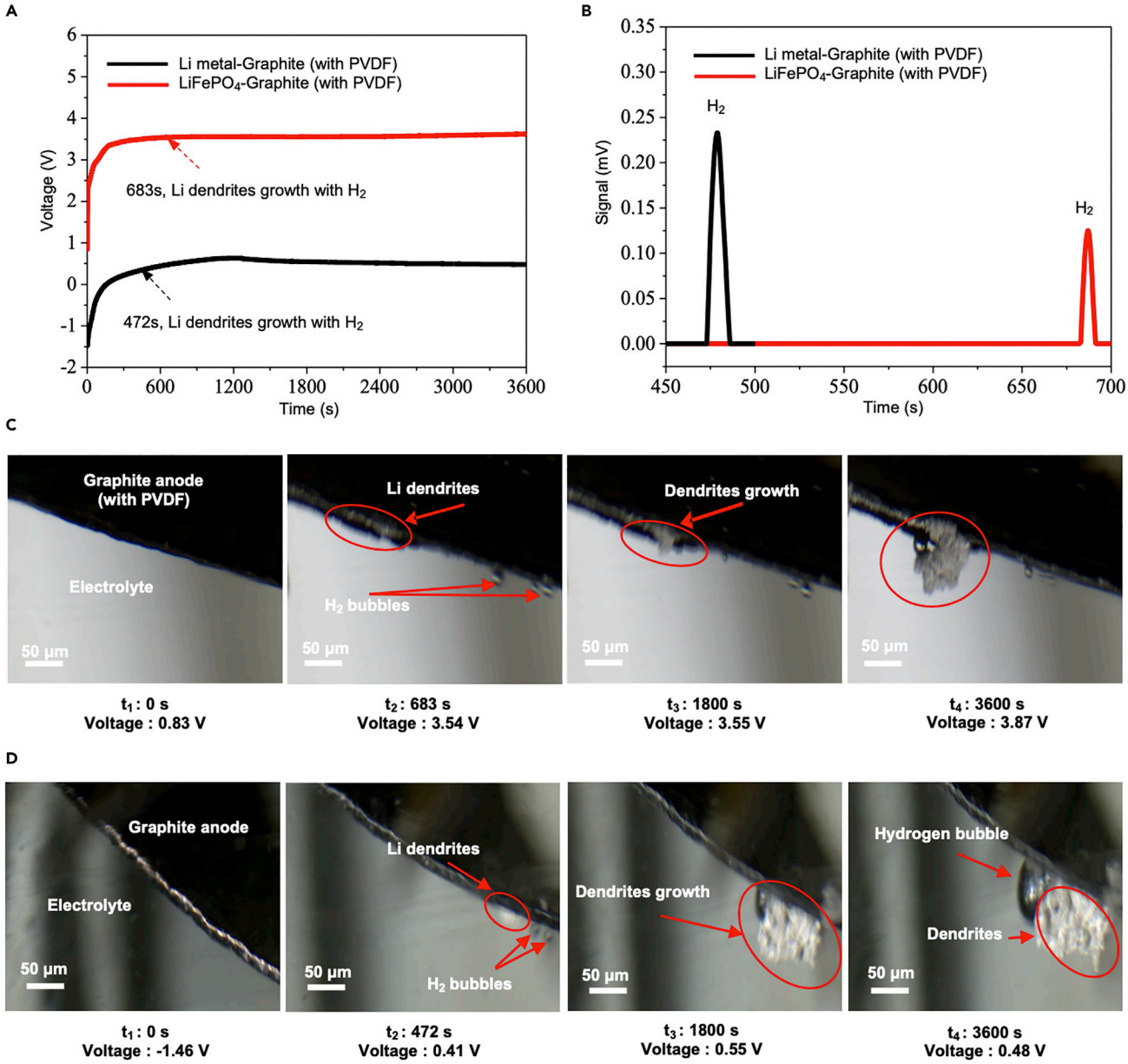

Figure 2. *In Situ* Experiments of Li Dendrite Detection and H_2 Gas Capture with Presence of Polymer Binder

(A) Voltage-time profiles of self-assembled LIBs (anode area of 3 cm^2 and charge current of 3 mA).

(B) H_2 gas was captured at 683 and 472 s for the two kinds of assembled LIBs through automatic gas chromatography detecting.

(C) Microscopy images of graphite anode surface during the charging process. The cell consists of a $LiFePO_4$ cathode and graphite anode (with PVDF binder).

(D) Microscopy images of graphite electrode surface during the charging process. The cell consists of a Li-metal electrode and graphite electrode (with PVDF binder).

approximately 0.3 V. H_2 signal and bubbles were detected (Figure 2B) and observed (Video S2) at that time.

Figure 2C shows optical images on graphite anode of $LiFePO_4$-graphite cell at different times and voltages. The Li dendrite continued to grow to micro-scale size and were accompanied by H_2 bubbles from 683 to 3,600 s. Figure 2D shows optical images of Li-metal-graphite cell at different times and voltages. The same as

$LiFePO_4$-graphite cell, with Li dendrites growing, H_2 gas is generated from the root of Li dendrites where metal react with polymer binder in graphite electrode and gathered into big H_2 bubbles. Above experimental results demonstrate that whether in overcharge or normal charge conditions, H_2 gas is immediately generated once Li dendrites start growing with presence of PVDF binder.

To further exclude the joule heat effect on Li metal-PVDF reaction during charging caused by internal resistance, thermal simulation of the self-assembled cell was conducted based on finite element method. The anode and cathode electrodes were inserted in the electrolyte (Figure S7). The effective anode and cathode areas were about 3 cm^2, and the charging current was set as 3 mA (1 mA cm^{-2}). The whole charging process was about 1,900 s. Figure S8 shows the simulated temperature variation of the cell from 0 to 1,900 s. During charging, the simulated maximum temperature (Max), average temperature (Ave), and minimum temperature (Min) increased at almost the same rate. The cell temperature variation in different areas were almost the same, by ~0.22 K from 0 to 1,900 s. Considering the ambient temperature was about 20°C, the maximum temperature was about 20.22°C. Figure S9 shows the temperature field mapping of the cell at different time points. The temperature near the $LiFePO_4$ cathode was higher than that of the graphite anode as more heat was emitted near the $LiFePO_4$ cathode. It is obvious that the temperature variation is very small and impossible to cause localized heat, thus affecting the reaction.

A similar H_2 gas generation process was observed for the assembled $LiFePO_4$-graphite cell with different polymer binders (SBR and CMC based, pre-dried by vacuum drier, graphite:carbon black:CMC:SBR = 90:4:3:3), as shown in Figure S10; Video S3. For the $LiFePO_4$-graphite cell (SBR and CMC based), charge process starts from 0% SOC at 0s, and Li dendrite growth was observed at approximately 437 s, while the cell voltage was approximately 3.5 V. The Li dendrite growth starting time was shorter than that of $LiFePO_4$-graphite cell (PVDF based), which may be due to the higher reaction kinetic of SBR and CMC with Li metal than that of PVDF. From Video S3, active materials on graphite anode continuously split off with Li dendrites growing and H_2 gas generation, as the SBR and CMC binder is gradually consumed up with Li metal.

In Situ Experiments of Li Dendrite Detection without Polymer Binder

To exclude the interferences of electrolyte reduction and other substances, we assembled another two LIBs ($LiFePO_4$-Cu and $LiFePO_4$-graphite cells) without any polymer binder. The graphite and Cu foil anodes in both cells contain no polymer binder, and the mass ratio of graphite:carbon black was 8:1. Figure 3A shows the cells' voltage profile during charging, both cells start from 0% SOC at 0 s. For $LiFePO_4$-graphite cell, Li dendrite growth was observed at 1,080 s, while the cell voltage was about 3.6 V. The time interval was higher than that of $LiFePO_4$-graphite cell with polymer binder (Figure 2A) due to different selected areas for *in situ* observation. For $LiFePO_4$-Cu cell, Li ions were directly plated on Cu foil surface to form Li metal. However, due to the observation limitation of optical microscope, Li dendrite growth (~ 30 μm diameter) was observed at about 120 s while the cell voltage was about 3.6 V. Figure 3B shows the H_2 detection result. For both $LiFePO_4$-graphite and $LiFePO_4$-Cu cells, no H_2 gas signal was detected from 0 to 3,600 s, which means no H_2 gas was released. Figures 3C and 3D show the optical images of Li dendrite growth on Cu foil of $LiFePO_4$-Cu cell and graphite anode of $LiFePO_4$-graphite cell at different times and voltages, respectively. With Li dendrite growing, no H_2 bubble

Please cite this article in press as: Jin et al., Detection of Micro-Scale Li Dendrite via H_2 Gas Capture for Early Safety Warning, Joule (2020), https://doi.org/10.1016/j.joule.2020.05.016

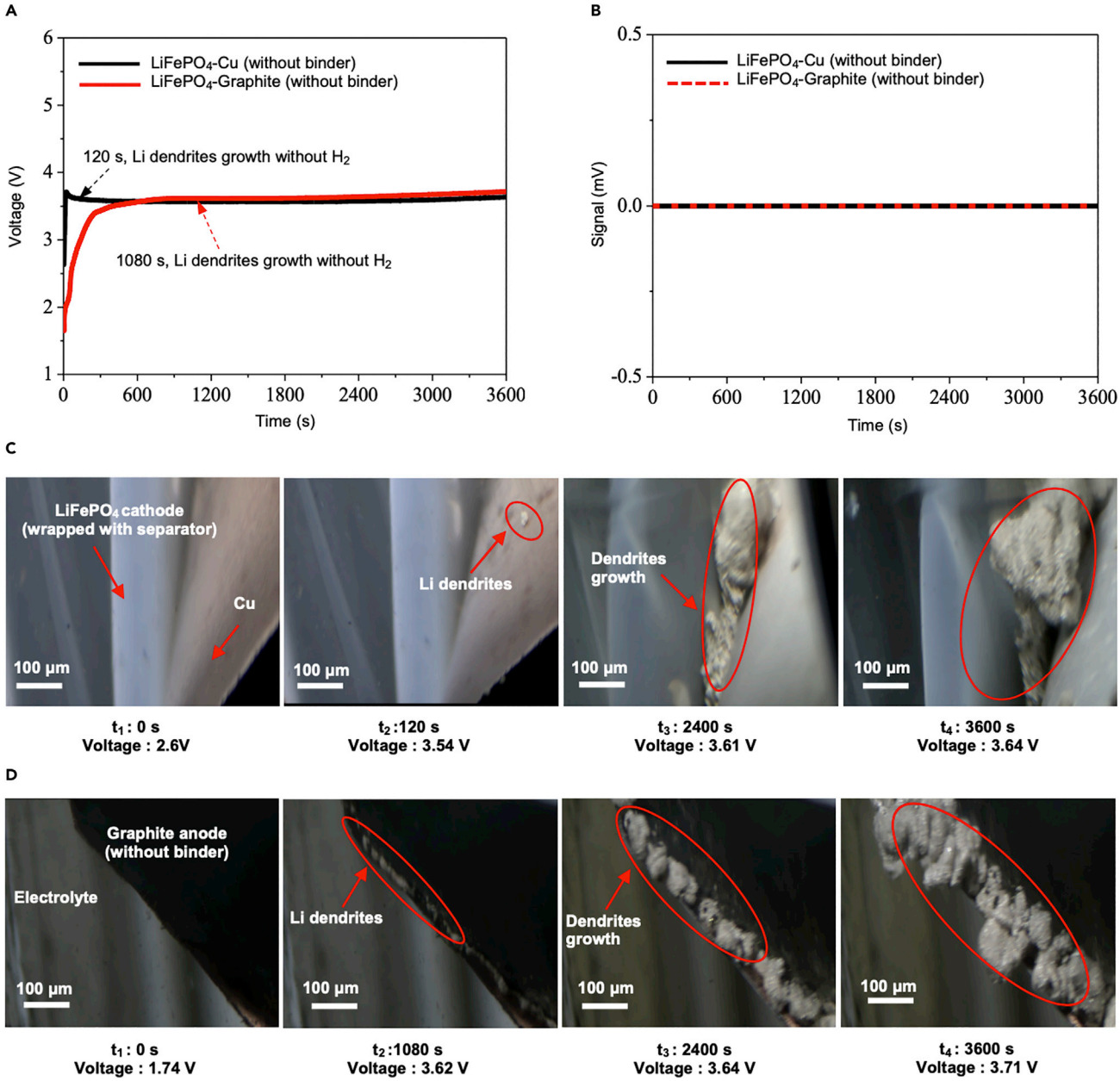

Figure 3. *In Situ* Experiments of Li Dendrite Growth without Polymer Binder

(A) Voltage-time profiles of self-assembled LIBs (anode area of 3 cm^2 and charge current of 3 mA).

(B) Automatic gas chromatography results show no H_2 gas signal detected.

(C) Microscopy images of the Cu foil surface during the charging process. The cell consists of a $LiFePO_4$ cathode and pure Cu foil current collector (without polymer binder).

(D) Microscopy images of the graphite surface the charging process. The cell consists of a $LiFePO_4$ cathode and graphite anode (without polymer binder).

was observed for both cells. The experimental videos can be seen in Videos S4 ($LiFePO_4$-Cu) and S5 ($LiFePO_4$-graphite).

Above experimental results demonstrate that during the charging process, even though Li dendrites started growing, no H_2 bubbles was observed or detected with absence of polymer binder in anodes. The electrolyte (EC, EMC and PC) can still

maintain its chemical stability under above cell voltages[57] and room temperature ambient.[58] The results also prove that the H_2 bubbles come from the Li-metal binder reaction, and the EC, EMC and PC electrolyte or other substances do not take part in H_2 gas generation.

The Theoretical Calculation of H_2 Gas Generation and Size of Li Dendrite

It has been proved that the H_2 gas comes from the reaction of metallic Li and polymer binder. To understand how much H_2 gas can be released for capture and the corresponding size of Li dendrite formation in our experiment, here, we theoretically calculate the amount of H_2 gas. The metallic Li-PVDF reaction can be expressed by the following equation:

$$-CH_2 - CF_2 + Li \rightarrow LiF + -CH = CF- + 0.5H_2 \qquad \text{(Equation 1)}$$

Similarly, this dehydrofluorination reaction also occurs on the SBR and CMC-based anode with H_2 generation during overcharging. In our experiments, argon gas continuously flows through the pipe with the flow rate pre-set to be 5 mL min^{-1} to carry the mixed gases into gas chromatograph. The injection volume of the mixed gases during one determination cycle was pre-set to be 1 mL. The extremely low solubility and dissolution rate of H_2 in electrolyte benefit fast H_2 diffusion.[59,60] While the H_2 gas concentration reaches 500 ppm in the mixed gases during one determination cycle, it can be detected by the gas chromatograph. Thus, the minimal H_2 content can be calculated to be 4.5×10^{-5} mg at room temperature (20°C) under one bar pressure. This is equivalent to a Li-metal particle with a radius of ~50 μm (approximately 2.8×10^{-4} mg) plated on the graphite anode, which can result in detectable H_2 generation by gas chromatography. In practice, the deposited Li will be distributed in different areas (Li saturated parts) on graphite anode. Thus, the actual size of Li will be smaller than 50 μm. It is noted that the first H_2 signal detected by gas chromatography is very important, which means Li metal starts growing. It can be regarded as an early warning indicator. In our experiments, the detection precision depends on the detectable minimal H_2 concentration by gas chromatography.

Overcharge Experiments of LIB Pack with H_2 Gas Capture

To verify the efficacy of proposed H_2 gas capture method in practical applications, we conducted overcharge experiment of commercial battery pack. As shown in Figure 4A, the overcharge experiment of $LiFePO_4$ battery pack was conducted in a real BESS cabin environment (approximately 86 m^3). The optical image of real experimental environment is shown in Figure S11. Six gas sensors were arranged immediately above the pack to detect concentration changes of H_2, CO, CO_2, HCL, HF, and SO_2. Two high-resolution optical cameras were installed for observation from different perspectives. A K-type thermocouple was attached to the upper surface of the pack (the upper cover was removed) to measure the surface temperature. Real-time gas detection was carried out under overcharge conditions with a constant current of 0.5 C (172 A) on a fully charged $LiFePO_4$ battery pack (8.8 kWh, consisting of 32 single prismatic cells with aluminum package). The rated voltage of the battery pack was 25.6 V. According to the calculation above, the theoretical H_2 yield can reach 4.48 g if the PVDF binder (3 wt % of graphite anode) in the $LiFePO_4$ battery pack completely reacts with the metallic Li. Taking the volume of the BESS cabin into account, the H_2 gas concentration will reach a theoretical value of approximately 52.09 mg m^{-3} (~580 ppm).

Figure 4B shows the voltage profile and pack surface temperature variation during the charging process. The battery pack was continuously overcharged to fire

Please cite this article in press as: Jin et al., Detection of Micro-Scale Li Dendrite via H_2 Gas Capture for Early Safety Warning, Joule (2020), https://doi.org/10.1016/j.joule.2020.05.016

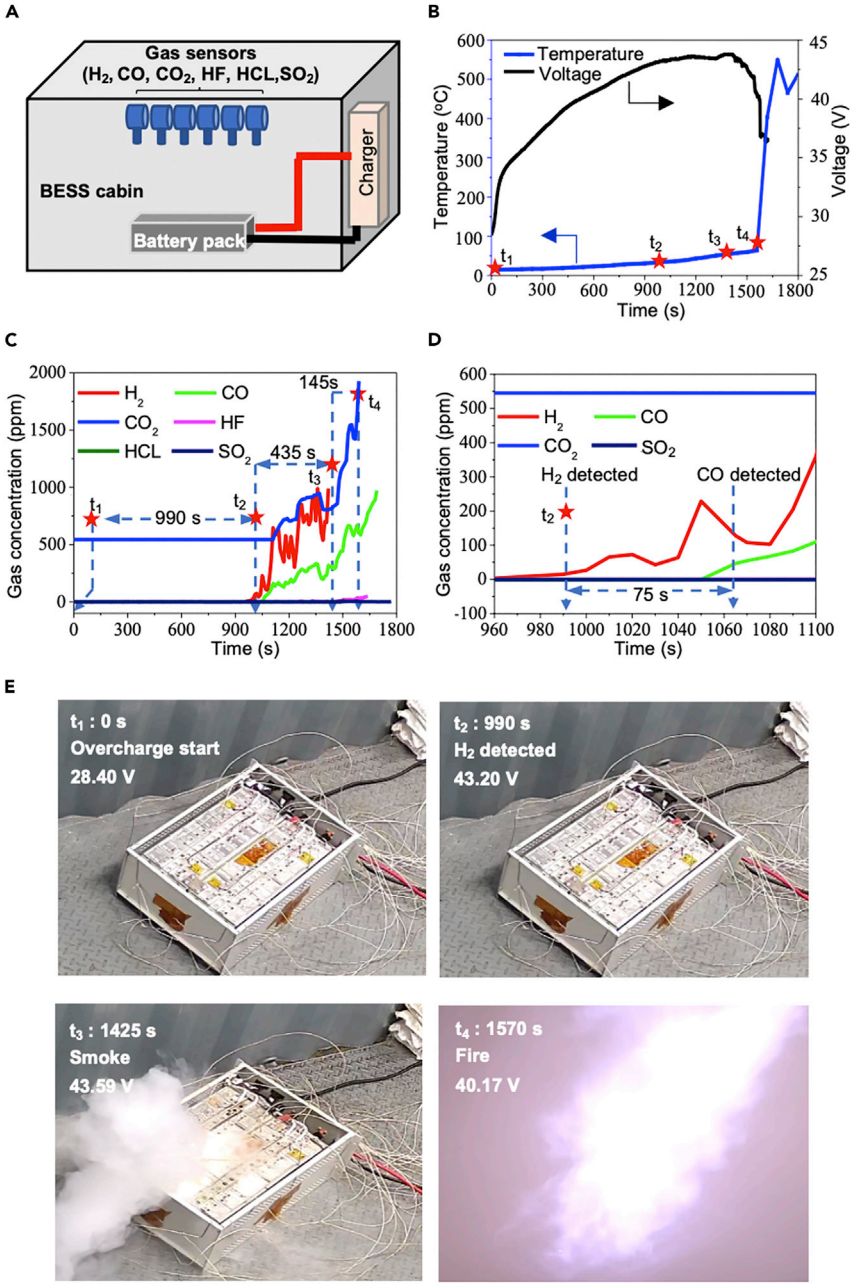

Figure 4. Overcharge Experiment of a $LiFePO_4$ Battery Pack (8.8 kWh) with Online Detection of Six Gases in a Real BESS Cabin

(A) Illustration of the experimental environment in a real BESS cabin. Six gas (H_2, CO, CO_2, HF, HCL, and SO_2) sensors were set above the battery pack.

(B) Voltage profile and surface temperature variation of the $LiFePO_4$ battery pack during overcharging (charge current rate: 0.5 C).

(C) Gas concentration variation of six kinds of gas 0–1,800 s.

(D) Enlarged gas concentration curves 960–1,100 s.

(E) Optical image of $LiFePO_4$ battery pack at different time. t_1 = 0 s, the initial time of overcharge; t_2 = 990 s, H_2 gas was detected; t_3 = 1,425 s, smoke appearance; t_4 = 1,570, fire explosion.

explosion, which was approximately 43 V (1.68 times the rated voltage value). Here, we select four special time points to better elaborate the developing process as t_1, t_2, t_3, and t_4. t_1 = 0 s stands for the initial charging start time point; t_2 = 990 s stands for the H_2 detected time point; t_3 = 1,425 s stands for the smoking appearance time point; t_4 = 1,570 s stands for the fire explosion time point. Concentration variations of the six gases detected in our experiment are shown in Figures 4C and 4D. Figure 4E presents the optical images at different time points of t_1–t_4. The whole overcharge process was recorded in Video S6.

The battery pack (100% SOC) was overcharged from 28.40 V at t_1 (0 s) with an initial surface temperature of 28.4°C (Figure 4B). With overcharging, Li dendrites continuously grow on the graphite anode and react with the PVDF binder, thus generating H_2 gas. H_2 overflowed through the safety valves of the aluminum battery packages and was the first gas to be captured at early time point of t_2 = 990 s, as seen from Figure 4C. At this time point, no smoke was observed (Figure 4E), and the surface temperature was just 35.6°C as seen in Figure 4B. At t_3 time point of 1,425 s, a dense column of smoke suddenly appeared (Figure 4E), gradually spreading to fill the whole space of the cabin and blocking the camera, and the pack surface temperature was only 55.8°C (Figure 4B). At t_4 time point of 1,570 s, a fire explosion abruptly occurred when the surface temperature was approximately 64.3°C. Then the surface temperature dramatically increased to 548.7°C in approximately 80 s, and the whole battery pack was completely burned (Figure 4E).

From the concentration variation curves as seen in Figure 4C, the concentration value of H_2, CO, and CO_2 (the measurement ranges are 0–1,000, 0–1,000, and 0–2,000 ppm, respectively) increased significantly from time point of t_2 = 990 s (H_2 detected) to t_3 = 1,425 s (dense smoke appeared). HCL, HF, and SO_2 maintained their values at zero for a fairly long time and slightly increased after the battery pack caught fire at time point of t_4 = 1,570 s. It is noted that H_2 was captured 435 s before smoke appearance and 580 s before the pack catching fire, thus providing precious time for personnel evacuation and fire prevention.

For better comparison, the concentration variation curves (from 960 to 1,100 s) of the six gases are enlarged (Figure 4D). Here, we set a consistent warning value as 20 ppm for H_2 and CO and 50 ppm increment value for CO_2. H_2 was the first to be captured at 990 s, CO was the second one at 1,065 s, and CO_2 was the third one at 1,120 s (Figure 4C). It is obvious that the warning time of H_2 is 75 s earlier than CO and 130 s earlier than CO_2. The time of the gas captured is the most important parameter. The earlier to be captured, the more time will be reserved for safety action, such as personnel evacuation and cutting off charger power. It is worth noting that, when H_2 was detected at 990 s, the surface temperature of the pack remained very low (35.6°C), much lower than the common temperature warning value of 60°C, which also reflects the unreliability of current battery safety warning technique by surface temperature. In general, above results verify the superiority of H_2 capture method than other five gases and surface temperature in achieving early battery safety warning. It also proves the effectiveness of Li dendrite growth detection by H_2 gas capture. In our experiment, Li dendrites start growing on graphite anode and reacting with polymer binder thus generating H_2 gas much earlier than CO and other gas from SEI decomposition. That is why the detection time of H_2 is earlier than other gases. Considering the time delay of H_2 gas aggregation and leakage from cell valve, the actual Li dendrite growth and H_2 generation time inside battery should be much earlier than t_2 (990 s).

Cell venting time can affect the detection of H_2 gas. The venting time of the first 12 cells is listed in Table S1. H_2 was immediately captured at 990 s after the first cell venting at 971 s. The H_2 captured time is associated with the first venting time of cells. Here, almost 10 min was reserved for early safety warning, which is long enough for precautions, such as personnel evacuation and cutting off chargers.

The H_2 capture method can also be applied to cells that have no safety valve, such as pouch cells. Here, overcharging experimental of pouch cells was conducted to verify the effect of H_2 capture. The battery pack consists of 72 $LiFePO_4$ pouch cells (48 Ah). The rated voltage of the pack was 38.4 V, and the total energy capacity was 11.1 kWh. The battery pack was overcharged at 0.5 C rate from 100% SOC. Figure S12A shows the cells swelling and deformation from 0 to 2,500 s. With overcharging process, deformation gets serious. As the package of pouch cell is made of aluminum plastic materials, it is easy to be cracked or broken with cell swelling. After cracking, a dense column of smoke is gradually spreading to fill the whole space of the cabin and blocking the camera. At about 2,319 s, a fire explosion abruptly occurred. Thermocouples are placed on top, left, and right surface of battery pack. Figure S12B shows the temperature variation during overcharging process. The surface temperature dramatically increased to 600°C in approximately 50 s, and the whole battery pack was completely burned. It is noted that when smoke appeared at 2,061 s, the surface temperature was just about 40°C. Figure S12C shows concentration variation of H_2 gas. It is obvious that the concentration value of H_2 (the measurement ranges are 0–1,000 ppm) increased significantly from time point of 1,485 s (H_2 captured). H_2 was captured 576 s earlier than smoke appearance (at 2,061 s) and 834 s earlier the pack catching fire (at 2,319 s). The time interval between H_2 capture and thermal runaway was 834 s, which is longer than prismatic cells with aluminum package.

In addition, to explore the H_2 gas diffusion characteristic in BESS cabin, another overcharge experiment was conducted on the same fully charged $LiFePO_4$ battery pack under a constant overcharge current of 0.5 C (172 A). H_2 gas sensors were directly mounted to the ceiling at 2-m intervals (named $Hydrogen_0$, $Hydrogen_2$, and $Hydrogen_4$), with $Hydrogen_0$ mounted right above the overcharged pack. The real experimental environment is shown in Figures S13 and S14, and the upper cover remained. Similar to the former overcharge experiment, the whole process underwent three phases (Figures S13C–S13F; Video S7): H_2 capture, smoke appearance, and fire explosion. The gas concentration variation curves of the H_2 by the three sensors are shown in Figure S13G (0–2,000 s) and enlarged in Figure S13H (980–1,120 s). H_2 was detected at 1,006 s by the $Hydrogen_0$ detector, 46 s earlier than $Hydrogen_2$, 83 s earlier than $Hydrogen_4$, 639 s earlier than smoke appearance, and almost 780 s earlier than fire explosion.

Results demonstrate that the H_2 gas diffusion along horizontal direction will cause detection time delay. In practical application, H_2 sensor cannot be guaranteed to install right above the accidental battery pack, so several H_2 sensors are needed to cover the protected BESS area. For standard BESS cabin with length of 12 m, at least six H_2 gas sensors are necessary. For an electric vehicle with length variation from 4-6 m, two or three H_2 gas sensors are sufficient.

Safety Warning Experiments of LIBs Battery Cluster with H_2 Gas Capture

In real BESS condition, a crowd of battery packs connected to form a battery cluster for higher capacity. The H_2 gas detection environment will be more severe as other battery packs will cause physical blocking for gas diffusion. To further study the effectiveness of H_2 gas capture and safety warning under real-operating condition

Please cite this article in press as: Jin et al., Detection of Micro-Scale Li Dendrite via H_2 Gas Capture for Early Safety Warning, Joule (2020), https://doi.org/10.1016/j.joule.2020.05.016

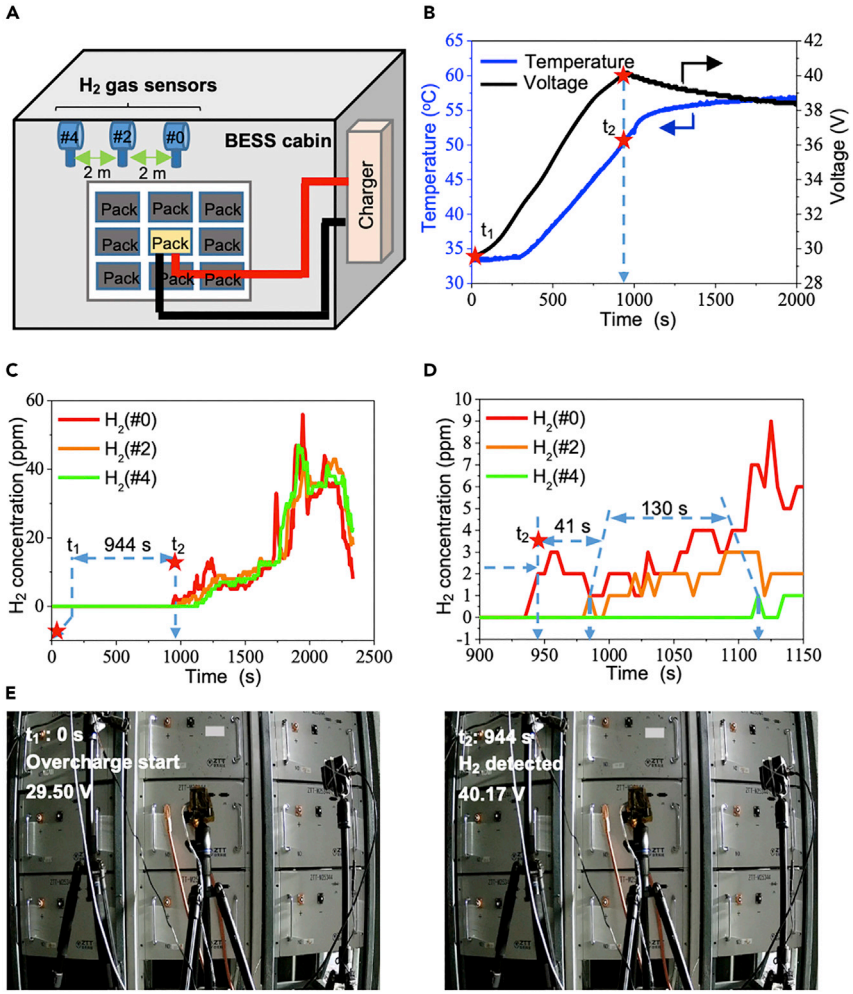

Figure 5. Safety Warning Experiment of a $LiFePO_4$ Battery Cluster (9 Battery Packs, 79.2 kWh) with H_2 Gas Capture

(A) Illustration of the experimental environment in a real BESS cabin, and three H_2 gas sensors were set at varying distances.

(B) Voltage profile and surface temperature variation of the $LiFePO_4$ battery cluster during overcharging (charge current rate: 0.5 C).

(C) H_2 gas concentration variation curves of three sensors 0–2,500 s.

(D) Enlarged H_2 gas concentration variation curves of three sensors 900–1,150 s.

(E) Optical image at the initial time of t_1 = 0 s and t_2 = 994 s when H_2 gas was captured and the charging process was stopped.

(battery pack fully stacked), here, we carried out a safety warning experiment involving nine fully charged $LiFePO_4$ battery packs (79.2 kWh and consisting of 288 single cells) in the BESS cabin, as shown in Figure 5A (optical image can be seen in Figure S15), to explore whether H_2 diffusion would be hindered by other packs. The packs were put in three layers to simulate the real-operating conditions with more sufficient heat accumulation and shelter. Three H_2 sensors named H_2 (#0), H_2 (#2), and H_2 (#4) were attached to the ceiling of the cabin at 2-m intervals, as shown, with H_2 (#0) attached right above the central pack.

The central battery pack was overcharged under a constant current of 0.5 C (172 A). In addition, a K-type thermocouple was attached to the upper surface (under the

upper cover) of the overcharged pack. Figure 5B shows voltage profile and the pack surface temperature variation during the whole process. Here, we select two special time points to better elaborate the developing process as t_1 and t_2. t_1 = 0 s stands for the initial charging start time point with 100% SOC; t_2 = 944 s stands for the first H_2 detected time point by H_2 (#0) sensor.

The overcharge process started at 0 s (t_1) and was terminated as soon as H_2 gas was detected by the H_2 (#0) sensor at 944 s (t_2). From Figure 5B, the surface temperature of the pack only increased from 33.4°C to a relatively low value of 51.9°C when H_2 was first captured at t_2 and gradually tended to be stable once the charging process was terminated, indicating that the heat accumulation inside the pack was suppressed as well. Concentration variations of H_2 gas detected by the three sensors are shown in Figure 5C (0–2,500 s) and are enlarged in Figure 5D (900–1,150 s). With overcharging process, H_2 gas diffused and was successively captured by H_2 (#0) at 944 s, H_2 (#2) at 985 s, and H_2 (#4) at 1,115 s. Figure 5E shows the optical images at time points of t_1 and t_2. As shown, neither smoke nor fire was observed (Video S8). By cutting off the charger power immediately once H_2 gas is captured, the Li dendrite growth process inside battery was prevented from further dendrite-shorted accident, and heat accumulation can be instantly suppressed in the meantime. The above experimental results indicate that even blocked by other packs in a real BESS cabin, the H_2 gas can still serve as an early warning indicator. As presented in Figures 4 and 5, in practical application, the proposed H_2 capture method is utilized for safety warning based on reaction between Li-metal and polymer binder. The purpose of Li dendrite detection here is to eliminate the occurrence of thermal runaway as early as possible.

While for electric vehicles, commercial LIB may not rupture under fast charging and low-temperature charging, so it might be difficult for the proposed method to detect Li dendrite growth during fast charging or low-temperature charging in commercial cells. If the commercial cells vent during fast charging or low-temperature charging, the proposed H_2 capture method works. Without venting, an effective solution is embedding a small H_2 sensor inside the battery for early Li dendrite detection. However, it will inevitably increase the cost.

DISCUSSION

We developed a sensitive detection method for Li dendrite growth in LIBs by H_2 gas capture for early safety warning. The smallest amount of metallic Li dendrites that can be detected is only 2.8×10^{-4} mg. Through gas detection experiments with a $LiFePO_4$ battery pack in a real BESS cabin, H_2 gas was found to be the most sensitive gas for detection and was captured much earlier than the other five gases that were detected online. A safety warning experiment with a $LiFePO_4$ battery cluster verified that even sheltered by other packs, H_2 gas can still be detected in the early stage. The Li dendrite growth and thermal accumulation process inside battery can be totally prevented by cutting off the charger at the time H_2 gas is captured, with neither smoke nor fire observed. Our H_2 gas capture technique provides an effective detection method of micron-scale Li dendrite formation for early safety warning and will improve the safety level of LIB systems.

EXPERIMENTAL PROCEDURES

Resource Availability

Lead Contact

Further information and requests for resources and reagents should be directed to and will be fulfilled by the Lead Contact, Yi Cui (yicui@stanford.edu).

Materials Availability

This study did not generate new unique reagents.

Date and Code Availability

This study did not generate or analyze(datasets or code).

Fabrication of the *In Situ* Experimental Platform

The *in situ* experimental platform includes three parts: self-assembled LIB cells, gas chromatography, and optical microscopy. The self-assembled LIB cell consisted of a cathode electrode, anode electrode, EC (35%), EMC (60%) and PC (5%) electrolyte, and separator. All the above materials were sealed in a 20 mL glass bottle. A silicon rubber plug with two through holes was used as the cap of the glass bottle. One hole was connected with the argon carrier gas, and one hole was connected with the gas chromatography instrument. Gas chromatography used as an automatic detection model. The cathode (3 cm^2) and anode (3 cm^2) materials were pre-dried in a vacuum oven for 48 h to remove moisture contamination. The charge current was 3 mA.

H_2 Capture Process by Gas Chromatography Instrument

High purity argon (99.999%) is used as carrier gas with the flow rate pre-set to be 5 mL min^{-1}. Argon gas continuously flows through the pipe to carry the mixed gases generated by the assembled LIB into gas chromatograph for H_2 capturing. The injection volume of the mixed gases during one determination cycle of gas chromatography was pre-set to be 1 mL. The gas intake gate automatically closes after the mixed gases (1 mL) are injected into gas chromatography. H_2 gas concentration should be at least 500 ppm in the mixed gases during one determination cycle for the gas chromatograph to detect.

Parameters of the $LiFePO_4$ Battery Pack

The $LiFePO_4$ battery pack used here consisted of 32 single cells. The rated voltage is 25.6 V, and the rated capacity is 8.8 kWh. The electrolyte inside the battery pack is EC (35%), EMC (60%) and PC (5%). The anode electrode contains graphite, PVDF, and carbon black, and the mass ratio of graphite:carbon black:PVDF is 90:7:3.

Calculation of Li-Metal Particle Diameter While Sensing H_2 Gas

The H_2 concentration should be at least 500 ppm in the mixed gases generated by the assembled LIB to be detected during one determination cycle with the gas chromatograph. The injection volume of the mixed gases during one determination cycle of gas chromatography was pre-set to be 1 mL. The metallic Li involved in the reaction (Equation 1) should be at least 2.86×10^{-4} mg (4.09×10^{-5} mol), indicating that approximately 4.09×10^{-5} mol Li ions from the cathode (Equation 2) are reduced into a metallic state (Equation 3) on the graphite anode during overcharging:

$$LiFePO_4 - xLi^+ - xe^- \rightarrow xFePO_4 + (1 - x)LiFePO_4 \quad \text{(Equation 2)}$$

$$xLi^+ + xe^- \rightarrow xLi \quad \text{(Equation 3)}$$

The number of electrons involved in this reduction reaction is calculated to be 2.46×10^{19} (4.09×10^{-5} mol $\times$ $6.02 \times 10^{23} \cdot mol^{-1}$), which is 3.94 C (or 1.09 mAh). This is equivalent to a Li-metal particle with a radius of ~50 μm plated on the graphite anode.

SUPPLEMENTAL INFORMATION

Supplemental Information can be found online at https://doi.org/10.1016/j.joule.2020.05.016.

ACKNOWLEDGMENTS

Y.J. acknowledges support from the National Natural Science Foundations of China (grant 51807180).

AUTHOR CONTRIBUTIONS

Conceptualization, Y.J. and Y.C.; Methodology, Y.J., Z.Z., D.W. and X.J.; Investigation, Y.J., Z.Z., H.W., T.S., L.S., D.G., Y.L., F.T., and J.G.; Writing – Original Draft, Y.J., Z.Z., and Y.C.; Writing – Review & Editing, Y.J., Z.Z., X.J., and Y.C.; Funding Acquisition, Y.J.; Supervision, Y.J. and Y.C.

DECLARATION OF INTERESTS

The authors declare no competing interests.

Received: February 29, 2020
Revised: April 23, 2020
Accepted: May 26, 2020
Published: July 10, 2020

REFERENCES

1. Chu, S., Cui, Y., and Liu, N. (2016). The path towards sustainable energy. Nat. Mater. *16*, 16–22.
2. Sun, Y., Liu, N., and Cui, Y. (2016). Promises and challenges of nanomaterials for lithium-based rechargeable batteries. Nat. Energy *1*, 16071.
3. Dunn, B., Kamath, H., and Tarascon, J.M. (2011). Electrical energy storage for the grid: a battery of choices. Science *334*, 928–935.
4. Liu, H., Wei, Z., He, W., and Zhao, J. (2017). Thermal issues about Li-ion batteries and recent progress in battery thermal management systems: a review. Energ. Convers. Manag. *150*, 304–330.
5. Wang, Q., Sun, J., Yao, X., and Chen, C. (2005). Thermal stability of $LiPF_6$/EC+DEC electrolyte with charged electrodes for lithium ion batteries. Thermochim. Acta *437*, 12–16.
6. Lamb, J., Orendorff, C.J., Roth, E.P., and Langendorf, J. (2015). Studies on the thermal breakdown of common Li-ion battery electrolyte components. J. Electrochem. Soc. *162*, A2131–A2135.
7. Liu, K., Liu, Y., Lin, D., Pei, A., and Cui, Y. (2018). Materials for lithium-ion battery safety. Sci. Adv. *4*, eaas9820.
8. Li, J., Murphy, E., Winnick, J., and Kohl, P.A. (2001). Studies on the cycle life of commercial lithium ion batteries during rapid charge-discharge cycling. J. Power Sources *102*, 294–301.
9. Feng, X., Ouyang, M., Liu, X., Lu, L., Xia, Y., and He, X. (2018). Thermal runaway mechanism of lithium ion battery for electric vehicles: a review. Energy Storage Mater. *10*, 246–267.
10. Balakrishnan, P.G., Ramesh, R., and Prem Kumar, T.P. (2006). Safety mechanisms in lithium-ion batteries. J. Power Sources *155*, 401–414.
11. Belov, D., and Yang, M. (2008). Failure mechanism of Li-ion battery at overcharge conditions. J Solid State Electrochem *12*, 885–894.
12. Goodenough, J.B., and Kim, Y. (2010). Challenges for rechargeable Li batteries †. Chem. Mater. *22*, 587–603.
13. Feng, X., Fang, M., He, X., Ouyang, M., Lu, L., Wang, H., and Zhang, M. (2014). Thermal runaway features of large format prismatic lithium ion battery using extended volume accelerating rate calorimetry. J. Power Sources *255*, 294–301.
14. Basu, S., Hariharan, K.S., Kolake, S.M., Song, T., Sohn, D.K., and Yeo, T. (2016). Coupled electrochemical thermal modelling of a novel Li-ion battery pack thermal management system. Appl. Energy *181*, 1–13.
15. Kong, W., Li, H., Huang, X., and Chen, L. (2005). Gas evolution behaviors for several cathode materials in lithium-ion batteries. J. Power Sources *142*, 285–291.
16. Kumai, K., Miyashiro, H., Kobayashi, Y., Takei, K., and Ishikawa, R. (1999). Gas generation mechanism due to electrolyte decomposition in commercial Li-ion cell. J. Power Sources *81–82*, 715–719.
17. Larsson, F., Bertilsson, S., Furlani, M., Albinsson, I., and Mellander, B. (2018). Gas explosions and thermal runaways during external heating abuse of commercial lithium-ion graphite-$LiCoO_2$ cells at different levels of ageing. J. Power Sources *373*, 220–231.
18. Golubkov, A.W., Fuchs, D., Wagner, J., Wiltsche, H., Stangl, C., Fauler, G., Voitic, G., Thaler, A., and Hacker, V. (2014). Thermal-runaway experiments on consumer Li-ion batteries with metal-oxide and olivin-type cathodes. RSC Adv. *4*, 3633–3642.
19. Yang, Z., Zhang, J., Kintner-Meyer, M.C., Lu, X., Choi, D., Lemmon, J.P., and Liu, J. (2011). Electrochemical energy storage for Green Grid. Chem. Rev. *111*, 3577–3613.
20. Fernandes, Y., Bry, A., and de Persis, S. (2018). Identification and quantification of gases emitted during abuse tests by overcharge of a commercial Li-ion battery. J. Power Sources *389*, 106–119.
21. Hill, D., Gully, B., Agarwal, A., et al. (2013). Detection of off gassing from Li-ion batteries (Cleveland, USA: 2013 IEEE Energytech), pp. 142–149.
22. Eshetu, G.G., Grugeon, S., Gachot, G., Mathiron, D., Armand, M., and Laruelle, S. (2013). LiFSI vs. $LiPF_6$ electrolytes in contact with lithiated graphite: comparing thermal stabilities and identification of specific SEI-reinforcing additives. Electrochim. Acta *102*, 133–141.
23. Wang, Q., Ping, P., Zhao, X., Chu, G., Sun, J., and Chen, C. (2012). Thermal runaway caused fire and explosion of lithium ion battery. J. Power Sources *208*, 210–224.
24. Lu, L., Han, X., Li, J., Hua, J., and Ouyang, M. (2013). A review on the key issues for lithium-ion battery management in electric vehicles. J. Power Sources *226*, 272–288.
25. Li, H., Duan, Q., Zhao, C., Huang, Z., and Wang, Q. (2019). Experimental investigation on the thermal runaway and its propagation in the

large format battery module with $Li(Ni_{1/3}Co_{1/3}Mn_{1/3})O_2$ as cathode. J. Hazard. Mater. *375*, 241–254.

26. Ribière, P., Grugeon, S., Morcrette, M., Boyanov, S., Laruelle, S., and Marlair, G. (2012). Investigation on the fire-induced hazards of Li-ion battery cells by fire calorimetry. Energy Environ. Sci. *5*, 5271–5280.

27. Rahimi-Eichi, H., Ojha, U., Baronti, F., and Chow, M.Y. (2013). Battery management system an overview of its application in the smart grid and electric vehicles. IEEE Industrial Electronics Magazine *7*, 4–16.

28. Hong, J., Wang, Z., and Yao, Y. (2019). Fault prognosis of battery system based on accurate voltage abnormity prognosis using long short-term memory neural networks. Appl. Energy *251*, 113381.

29. Xiong, R., and Shen, W. (2019). Advanced Battery Management Technologies for Electric Vehicles (Wiley).

30. Xiong, R., Tian, J., Shen, W., and Sun, F. (2019). A novel fractional order model for state of charge estimation in lithium ion batteries. IEEE Trans. Veh. Technol. *68*, 4130–4139.

31. Srinivasan, R., Carkhuff, B.G., Butler, M.H., and Baisden, A.C. (2011). Instantaneous measurement of the internal temperature in lithium-ion rechargeable cells. Electrochim. Acta *56*, 6198–6204.

32. Grandjean, T.R., Barai, A., Hosseinzadeh, E., Guo, Y., Mcgordon, A., and Marco, J. (2017). Large format lithium ion pouch cell full thermal characterisation for improved electric vehicle thermal management. J. Power Sources *359*, 215–225.

33. Esho, I., Shah, K., and Jain, A. (2018). Measurements and modeling to determine the critical temperature for preventing thermal runaway in Li-ion cells. Appl. Therm. Eng. *145*, 287–294.

34. Tripathi, A.M., Su, W.N., and Hwang, B.J. (2018). In situ analytical techniques for battery interface analysis. Chem. Soc. Rev. *47*, 736–851.

35. Zhu, Y., Xie, J., Pei, A., Liu, B., Wu, Y., Lin, D., Li, J., Wang, H., Chen, H., Xu, J., et al. (2019). Fast lithium growth and short circuit induced by localized-temperature hotspots in lithium batteries. Nat. Commun. *10*, 2067.

36. Zinth, V., von Lüders, C., Hofmann, M., Hattendorff, J., Buchberger, I., Erhard, S.V., Rebelo-Kornmeier, J., Jossen, A., and Gilles, R. (2014). Lithium plating in lithium-ion batteries at sub-ambient temperatures investigated by in situ neutron diffraction. J. Power Sources *271*, 152–159.

37. Wandt, J., Jakes, P., Granwehr, J., Eichel, R., and Gasteiger, H.A. (2018). Quantitative and time-resolved detection of lithium plating on graphite anodes in lithium ion batteries. Mater. Today *21*, 231–240.

38. Arai, J., Okada, Y., Sugiyama, T., Izuka, M., Gotoh, K., and Takeda, K. (2015). In situ solid state ^{7}Li NMR observations of lithium metal deposition during overcharge in lithium ion batteries. J. Electrochem. Soc. *162*, A952–A958.

39. von Lüders, C., Zinth, V., Erhard, S.V., Osswald, P.J., Hofmann, M., Gilles, R., and Jossen, A. (2017). Lithium plating in lithium-ion batteries investigated by voltage relaxation and in situ neutron diffraction. J. Power Sources *342*, 17–23.

40. Petzl, M., and Danzer, M.A. (2014). Nondestructive detection, characterization, and quantification of lithium plating in commercial lithium-ion batteries. J. Power Sources *254*, 80–87.

41. Qi, Y., and Harris, S.J. (2010). In situ observation of strains during lithiation of a graphite electrode. J. Electrochem. Soc. *157*, A741–A747.

42. Shboul, A.A., Shih, A., Oukachmih, M., and Izquierdo, R. (2019). ppb sensing level hydrogen sulphide at room temperature using indium oxide gas sensors. IEEE Sensors *2019*, 1–4.

43. Frisch, M.J., Trucks, G.W., Schlegel, H.B., et al. (2016). Gaussian (Wallingford CT: Gaussian, Incorp.).

44. Becke, A.D., and Axel, D. (1993). Density-functional thermochemistry. III. the role of exact exchange. J. Chem. Phys. *98*, 5648–5652.

45. Lee, C.T., Yang, W.T., and Parr, R.G. (1988). Development of the colle-Salvetti correlation-energy formula into a functional of the electron density. Phys. Rev. B Condens. Matter *37*, 785–789.

46. Mennucci, B., and Tomasi, J. (1997). Continuum solvation models: A new approach to the problem of solute's charge distribution and cavity boundaries. J. Chem. Phys. *106*, 5151–5158.

47. Barone, V., and Cossi, M. (1998). Quantum calculation of molecular energies and energy gradients in solution by a conductor solvent model. J. Phys. Chem. A *102*, 1995–2001.

48. Goodenough, J.B., and Park, K.S. (2013). The Li-Ion rechargeable battery: a perspective. J. Am. Chem. Soc. *135*, 1167–1176.

49. Fong, R., Sacken, U., and Dahn, J.R. (1990). Studies of Lithium intercalation into carbons using nonaqueous electrochemical cells. J. Electrochem. Soc. *137*, 2009–2013.

50. Dahn, J.R., Zheng, T., Liu, Y., and Xue, J.S. (1995). Mechanisms for lithium insertion in carbonaceous materials. Science *270*, 590–593.

51. Arora, P., White, R.E., and Doyle, M. (1998). Capacity fade mechanisms and side reactions in lithium-ion batteries. J. Electrochem. Soc. *145*, 3647.

52. Shin, J.S., Han, C.H., Jung, U.H., Lee, S.I., Kim, H.J., and Kim, K. (2002). Effect of Li_2CO_3 additive on gas generation in lithium-ion batteries. J. Power Sources *109*, 47–52.

53. Zhuang, G.V., Yang, H., Blizanac, B., and Ross, P.N. (2005). A study of electrochemical reduction of ethylene and propylene carbonate electrolytes on graphite using ATR-FTIR Spectroscopy. Electrochem. Solid State Lett. *8*, A441–A445.

54. Maleki, H., and Howard, J.N. (2006). Effects of over discharge on performance and thermal stability of a Li-ion cell. J. Power Sources *160*, 1395–1402.

55. Aurbach, D., Weissman, I., Zaban, A., and Dan, P. (1999). On the role of water contamination in rechargeable Li batteries. Electrochim. Acta *45*, 1135–1140.

56. Zheng, L.Q., Li, S.J., Lin, H.J., Miao, Y.Y., Zhu, L., and Zhang, Z.J. (2014). Effects of water contamination on the electrical properties of 18650 lithium-ion batteries. Russ. J. Electrochem. *50*, 904–907.

57. Xu, K. (2004). Nonaqueous liquid electrolytes for lithium-based rechargeable batteries. Chem. Rev. *104*, 4303–4417.

58. Botte, G.G., and Bauer, T.J. (2003). MRSST a new method to evaluate thermal stability of electrolytes for lithium ion batteries. J. Power Sources *119–121*, 815–820.

59. Shaharun, M.S., Mukhtar, H., and Dutta, B.K. (2008). Solubility of carbon monoxide and hydrogen in propylene carbonate and thermomorphic multicomponent hydroformylation solvent. Chem. Eng. Sci. *63*, 3024–3035.

60. Trinh, T., De Hemptinne, J., Lugo, R., Ferrando, N., and Passarello, J. (2016). Hydrogen solubility in hydrocarbon and oxygenated organic compounds. J. Chem. Eng. Data *61*, 19–34.